Analysis and Modification of Electronic Materials by MeV Ions*

T. A. Tombrello

Diuision of Physics, *Mathematics,* and *Astronomy*

California Institute of Technology

Pasadena, *CA 91125* USA

The use of MeV heavy-ion backscattering for the analysis of 111-V materials has allowed significant improvement of the elemental and depth resolution from that normally obtained with RBS. A time-of-flight detector system for such measurements is described here, as well as an example of its use in the analysis of InGaAs layers. Examples are also presented of the modification of the conductivity of amorphous carbon and $YBa_2Cu_3O_7$ single crystals. In both of these cases the incident ion does not stop within the sample; the change in conductivity arises solely from the damage produced by the ion; in the case of carbon from electronic excitation; in the case of the high T_c superconductor from collisions with nuclei in the material.

I. Introduction

In 1987 ? presented a paper in Caxambu that summarized our work on 111-V materials and devices. For the cases discussed it was possible to introduce electrically active dopant atoms by implanting MeV ions; the damage introduced in this process and its subsequent annealing were characterized by nuclear reaction profiling, channeling, x-ray scattering, and cross sectional TEM. The work discussed here extends that program, and different analysis and modification techniques will be presented in order to give a more complete picture of the optiors available to the experimenter.

For the case of the AlGaAs devices discussed in 1987, it was possible to use the $^{27}Al(p,\gamma)^{28}Si$ reaction to provide an absolute determination of the Al concentration, which could then be correlated with other material characteristics, e.g., lattice strain and band gap. In the extension of this program to InGaAs devices, there was no resonant iuclear reaction that could be used; thus, we had to improve the RBS method in order to obtain comparable results. This work is contained in Section II of this review.

In the case of materials modification discussed in 1987 the use of MeV ions allowed implantation doping into completed structures through the contact and photoresist layers. Because of the nature of the energy loss processes for such ions, minimal surface damage occurred. The cases to be discussed here require high energy bombardment for a different reason, the ion is intended to pass completely through the sample - only the damage along the ion's track is employed in the modification. Two examples are given of conductivity modification: in Section III for amorphous carbon films; and in Section IV for $YBa_2Cu_3O_7$ high T_c superconducting single crystals.

The goal of these examples and those presented in 1987 is the same; to enhance our ability to modify and to characterize electronic materials in order to understand better their fundamental properties and to apply them in a wider range of situations. It is certainly not my intention to claim a special place few for the use of MeV ions; however, as I shall discuss here, they do give

us unique tricks that we can add to those provided by the use of lower energy ions.

II. RBS witli MeV heavy ions

The Coulomb scattering of few MeV alpha particles has become a nearly universal technique to provide near surface analyses of elemental concentrations and damage. This has been true in large measure because of the simplicity of the experimental set up, i.e., a small scattering chamber and a surface barrier particle detector. Usually the detector is placed at nearly 180° to the incident beam, where the energy of the scattered particle is:

$$E_s = E_b \left(\frac{m_t - m_b}{m_t + m_b} \right) \qquad (1)$$

Here E_b is the energy of the beam particle just before it scatters and m_t and m_b are the masses of the target atom and beam ion, respectively.

Since we shall eventually compare the use of other beam ions, let us rewrite this formula as:

$$r = \frac{E_s}{E_b} = \left(\frac{1-x}{1+x} \right)^2 \quad \text{where} \quad x = \frac{m_b}{m_t} \ . \qquad (2)$$

Thus, our ability to resolve nearby target elements is determined by dr/dm_t. We shall rewrite this as

$$s = \frac{m_t}{r} \frac{dr}{dm_t} = \frac{4x}{1-x^2} \qquad (3)$$

These quantities are plotted versus x in Fig. 1. One sees that to get a kinematic resolution equivalent to ^{4}He on ^{28}Si (i.e., x = 1/7) for Ga, we would need a beam ion like boron or carbon. Unfortunately, the resolution of surface barrier detectors is quite poor for ions heavier than helium. So the improvement in the kinematic resolution is useless.
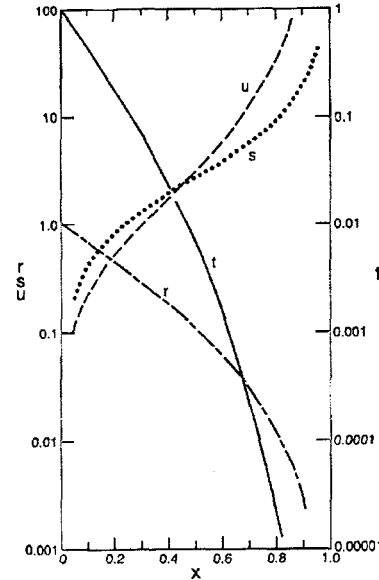

Figure 1: Parameters related to the kinematics for Rutherford backscattering at a laboratory angle of 180°. x is the ratio of the mass of the beam ion to the mass of the target atom. The parameters r, s, t, and u are defined in Section II of *the* text.

One could, of course, employ an electromagnetic spectrometer for the heavier ions, but that is made more complicated by the existence of a range of charge states of the scattered ions that even depends on the depth in target where the scattering occurs. In addition, what was an inexpensive, simple piece of apparatus has become complicated. We have chosen instead to measure the time of flight of the scattered ions between a pair of detectors. This allows their velocity to be determined and hence their energy.

The scattered ions pass through two thin carbon films ($\sim 5~\mu g/cm^2$) that are a known distance apart (83 cm for the data given here). The secondary electrons produced in each film are accelerated to a few keV and detected by microchannel plates. In the first version of this instrument[1] the first carbon film was tilted slightly with respect to direction of motion of the ion so that the electrostatic field in the accelerating structure could be relatively uniform. This tilt caused a small difference in flight time for particles that passed through different parts of the carbon film on their way to the second detector. Fig. 2 shows the various contributions to the energy resolution of the TOF detector. As you can see, the effect from the tilted carbon film dominates the resolution. Later in this section we shall present data from a modified version of this device; however, even

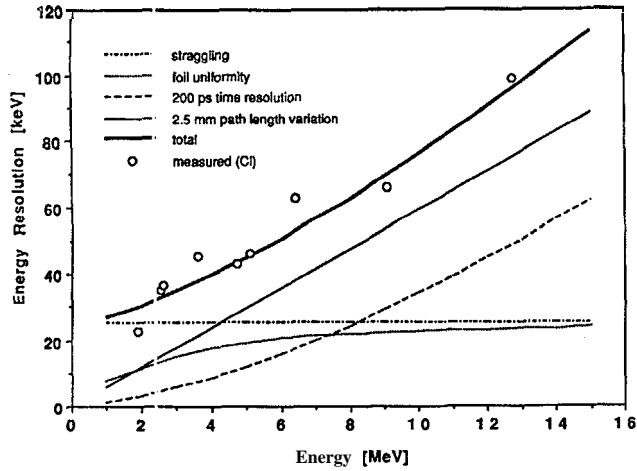in its original form excellent data could be obtained, as will be shown below.

Figure 2: The calculated energy resolution versus energy for ^{35}Cl ions include contributions from time resolution (200 ps), flight path differences (A $L/L = 0.3\%$ at $L = 830$ mm), and energy straggling and nonuniformity of the carbon film of the 1st detector. The points are measured values[1].

A spectrum obtained for the scattering of 25 MeV ^{35}Cl ions from a multi-element thin target are shown in Fig. **3.** Not only the elements are cleanly resolved, but also their isotopes, e.q., ^{63}Cu and ^{65}Cu and ^{107}Ag and ^{109}Ag.
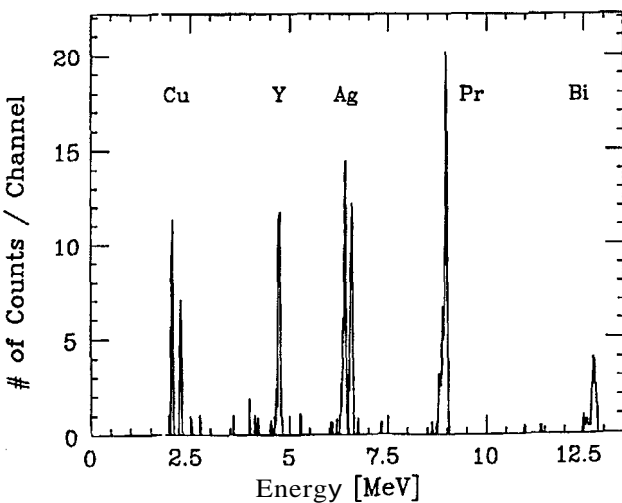

Figure 3: The energy spectrum for 25 MeV ^{35}Cl ions back scattered from a thin layer calibration target[1].
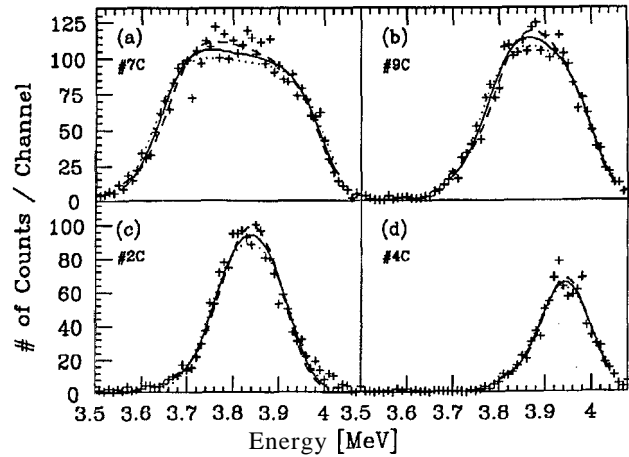

Figure 4: 15 MeV ^{35}Cl RBS spectra for In$_x$Ga$_{1-x}$As layers on GaAs covered with a 300 Å GaAs capping layer. Samples are tilted by 70° relative to the incident beam. (O° is perpendicular to the beam.) Solid line: best fit to the data. Dashed line: simulation for a layer 20 Å thinner. Dotted line: simulation for a layer 20 Å thicker[2].

Our first application of this detector was in measuring indium profiles in MBE-grown In$_x$Ga$_{1-x}$As/GaAs single quantum well structures and In Gal As layers on InAlAs buffer layers[2]. Fig. 4 shows the In RBS peaks for 15 MeV ^{35}Cl ions scattered from In$_x$Ga$_{1-x}$As layers on GaAs covered with a 300 A GaAs capping layer. The samples were tilted by 70° with respect to the incident beam; the detector was at an angle of 175°.

The RBS spectra were used to extract values of x and the thickness of the layers. These are given in Table 1, where the results are compared with the values obtained from the growth condition controls and photo-reflectivity measurements. With respect to the latter, different values of x would be obtained depending on whether the InGaAs layers were totally strained or completely relaxed. In general, the RBS data confirm that our determination of the growth conditions was really quite good, and the photo reflectivity associated with a strained InGaAs layer was the appropriate choice.

In order to improve the overall resolution of the TOF detector we changed the design of the front secondary electron detector. This modification is shown in Fig. 5, where the carbon film is now prependicular to the path of the scattered ions. The secondary electrons are accelerated and bent 180° by the magnetic field before striking the microchannel plate.

Fig. 6 gives the percent energy resolution for the original detector configuration (solid lines and squares)

Sample	Layer Thickness		InAs Mole Fraction				Cap Thickness
	From Growth [Å]	From RBS [Å]	From Growth	PR Strained	PR Relaxed	From RBS	From RBS [Å]
1C	100	60 ± 20	0.10	0.11	0.07	0.14 ± 0.05	240
2C	200	140 ± 20	0.10	0.08	0.06	0.06 ± 0.01	340
3C	300	280 ± 20	0.10	0.11	0.0S	0.10 ± 0.01	310
4C	100	80 ± 20	0.15	0.14	0.10	0.1S ± 0.04	300
5C	200	180 ± 20	0.15	0.13	0.10	0.13 ± 0.01	320
6C	300	280 ± 20	0.15	0.15	0.11	0.15 ± 0.01	320
7C	100	100 ± 20	0.20	0.18	0.13	0.16 ± 0.03	300
8C	200	200 ± 20	0.20	0.18	0.13	0.18 ± 0.02	320
9C	300	320 ± 20	0.20	0.17	0.12	0.16 ± 0.01	350

Table 1: Experimental results for the $In_xGa_{1-x}As$ samples with cap layers.

and the new front detector version (dotted lines) for scattered ^{35}Cl and ^{16}O ions of energy E. As you can see from the change in the slope of the dotted curve for higher energies (^{16}O ions), the effect of path differences no longer represents the dominant contribution to the energy. In fact, at this point there are essentially equal contributions from all the major sources, e.g., time resolution, straggling in the films, film uniformity, and path length variations. Thus, further improvement of the system will require a more substantial effort.

Considering the data shown in Fig. 3, why are we fighting so hard for better resolution? The curve labeled t in Fig. 1 gives the general idea. If we write the differential cross section for Coulomb scattering as:

$$\frac{d\sigma}{d\Omega}_{180° \text{ lab}} = \left[\frac{(Z_b/m_b)Z_t e^2}{4(E/m_b)}\right]^2 \frac{(1-x)^6}{(1+x)^2} \qquad (4)$$

We define $t = (1-x)^6/(1-x)^2$, which gives an indication of the price we pay in count rate for improving the kinematic resolution. (Here Z_b and Z_t are the atomic numbers of the beam and target atoms, respectively, and E is the energy of the backscattered particle.) Thus, increasing x to improve resolution (i.e., improving s) produces a very rapid decrease in counting rate. With that in mind, better resolution means that we can shorten the flight path, which improves the solid angle (and hence the counting rate) because it is proportional to the inverse square of the distance between the detectors. Our improvement in the resolution of the detector therefore has meant that the flight path can be decreased to 40 cm without degrading the performance of the system.

For completeness, we have plotted the effect of finite angular opening of the detector versus x:

$$\left(\frac{E_s}{E_b}\right)_{180°-\Delta \text{ lab.}} \simeq \left(\frac{1-x}{1+x}\right)^2 \left\{1 + \Delta^2\left[x + \frac{x^2}{(1-x)^2}\right]\right\} = k(\Delta) ;$$

$$u = \frac{1}{r\Delta}\frac{dk}{d\Delta} = 2\left[x + \frac{x^2}{(1-x)^2}\right] . \qquad (5)$$

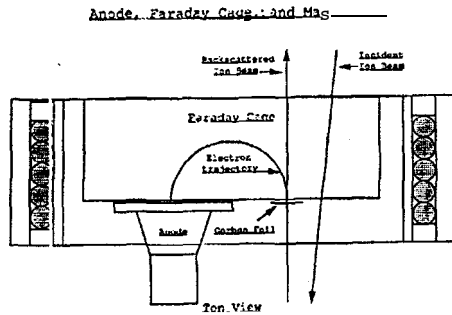Generally, the choice of x is not limited by u but by r, s, and/or t.

Figure 5: The modification of the front secondary electron detector using a magnetic field to bend the secondary electrons into the microchannel plate.
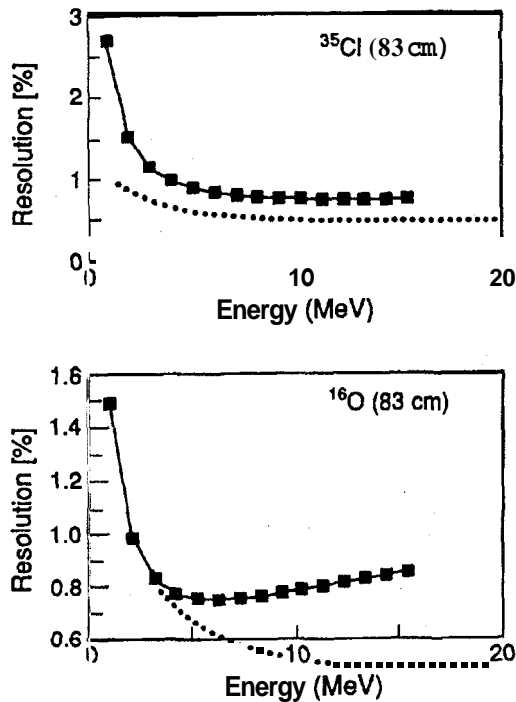

Figure 6: The percent energy resolution measured for scattered ^{15}Cl and ^{16}O ions in the original detector (solid lines and squares) and the modified detector (dotted lines). The energy is that of the scattered ion.

III. MeV ion induced conductivity changes in arnorphous carbon

Our interest in this research arose from the data shown in Fig. 7. In this case we found that while low energy ion Eombardment of evaporated carbon films increased the resistivity, high energy irradiation decreased it [3] These data suggest that low energy ions break up small, high conductivity graphite crystals in the material snd high energy ions create such crystals. Thus, there are two separate phenomena that may be

addressed: the mechanism by which the grains are created; and the fact that their production is determined by the irradiation gives us a way of probing the transition between a highly resistive starting material (amorphous carbon) and one that is nearly 10^4 time as conductive (polycrystalline graphite).

Starting with 1000 Å carbon films in their most resistive state, we irradiated them with ^{35}Cl ions at various energies as a function of fluence[4]. Data taken for 15 MeV ions are shows in Fig. 8 [4]. The extreme behavior of the conductivity versus temperature is made clearer in Fig. 9, where the data rise rapidly from zero at low fluences but show much less variation at high fliiences. The low fluence region was found to have a conductivity of the form:

$$\sigma = \sigma_0 \exp[-S(\Phi, E)T^{-1/2}] , \qquad (6)$$

where Φ is the ion fluence, E is the bombarding energy, and T is the absolute temperature. This is typical of Mott variable-range conduction, where electrons tunnel between randomly located, isolated conducting regions[5].
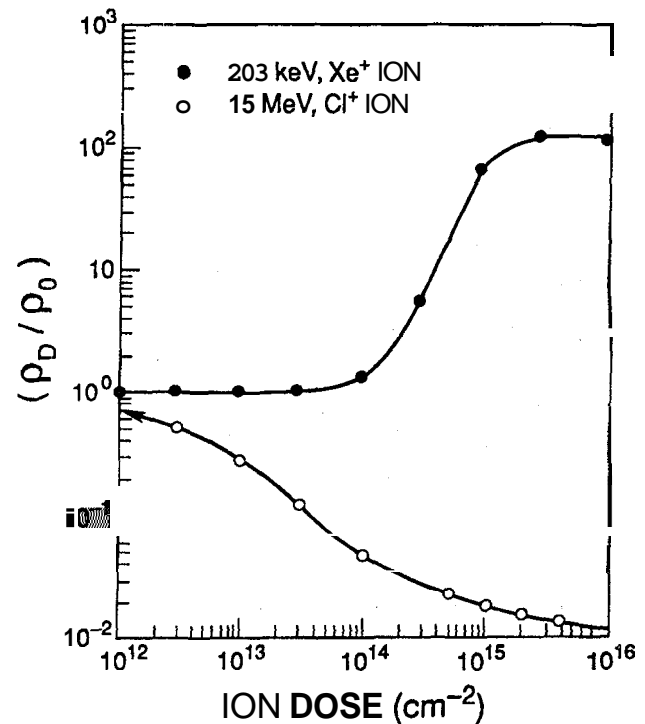

Figure 7: The ratio of the modified resistivity p and the pristine resistivity ρ_0 of an evaporated carbon film subjected to'' low and high energy irradiation, as a function of fluence (from ref. [3]).
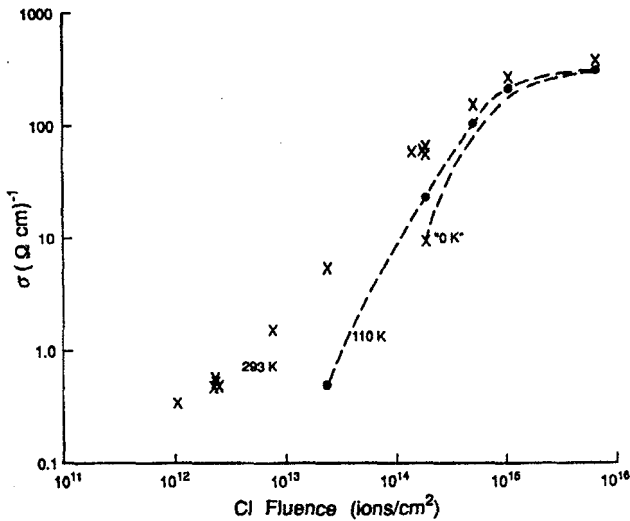
Figure 8: The room temperature conductivity measured for 15 MeV ^{35}Cl-ion-irradiated amorphous carbon films is plotted versus ion fluence. The curve labeled 110 K is the conductivity at that temperature. The points labeled "O K" are an extrapolation of the condutivity versus temperature to O K. (Taken from ref. [4].)
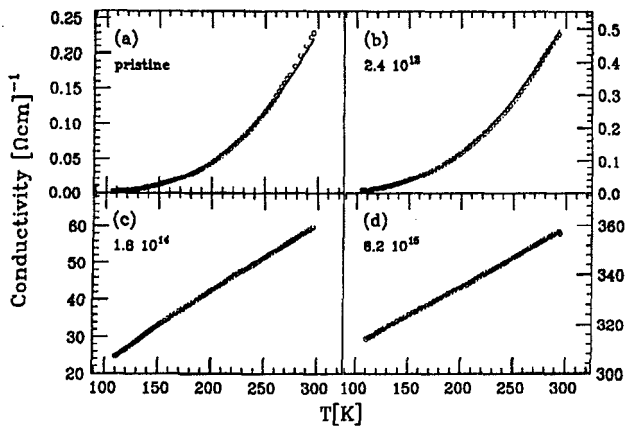

Figure 9: Conductivity versus temperature is plotted for 15 MeV ^{15}Cl irradiations. The circles are data; the solid lines are fits involving a mixture of hopping and metallic conduction, which is described in Section III of the text. (These results were taken from ref. [4].)

Examining the behavior of σ versus Φ in this region allows a cross section for the formation of the conducting grains to be obtained as a function of E. Since breaking a single carbon-carbon bond is not sufficient to form a graphite ring, the mechanism involved must simultaneously break several bonds in a local region. A model devised by Hedin et al. to explain the ion induced desorption of heavy molecules provides a convenient quantitative explanation for our purposes[6]. In an extended region (tens of Angstroms) around the MeV ion's path there are many energetic secondary

electrons (S-rays). The existence of this high electron fluence makes it possible to break simultaneously a number of carbon-carbon bonds in a local region. Since graphite is the most stable carbon compound, if enough bonds are broken at the same time a graphite ring can form. Using the cross section versus energy (e.g, 3 $\mathring{A}^2$ at 15 MeV), the model fit to the data gives a grain diameter of 6 f 3 Å with 8 f 3 bonds broken. This is close enough to what would be required to form one or two graphite rings - the smallest structure that would have the conducting properties of graphite.

At the highest fluences the measured conductivity has the form known for polycrystalline graphite, $\sigma_1 + \sigma_2 T$. ($\sigma_1 = 288$ [ohm cm]$^{-1}$ and $\sigma_2 = 0.234$ [ohm cm K]$^{-1}$.) This part of the conductivity is caused by the formation of connected chains of graphite rings. Fig. 10 gives the behavior versus ion fluence when these two contributions are added together as parallel circuits.
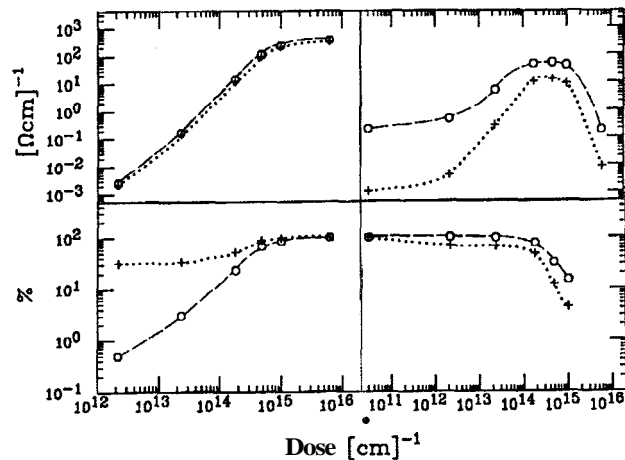

Figure 10: Comparison of chain (left) and tunneling (right) contributions to the total conductivity at 100 K (crosses) and 293 K (circles). Absolute values are shown at the top and percentages at the bottom. The dotted lines are intended only as a guide to the eye. (Taken from ref. [4].)

The growth of the chain conductivity has the form $1 - \exp[-(q\Phi)^2]$, which is what one obtains from percolation theory in three dimensions[7]. The parameter q can be related to the cross section for forming the conducting grain; at 15 Mev its value is 3 $\mathring{A}^2$, which agrees with the low fluence value obtained from the tunneling conductivity.

Overall, one sees that a consistent picture of the process has emerged that provides a quantitative estimate for the entire dose range, which corresponds to

nearly a 10^4 range of conductivities. The use of ion irradiation was an important factor, because by being able to use different ion energies and to vary the fluence continuously, the two parts of the mechanism could be disentangled.

IV. The effect of point defects in superconducting YBa₂Cu₃O₇ single crystals

In the "melting" transition of the Abrikosov magnetic flux line lattice in $YBa_2Cu_3O_7$ there is still uncertainty about the role played by the pinning of the lines to imperfect ons in the crystal (e.g., grain boundaries, twin planes, lattice defects). Since it has been difficult to start with "perfect" crystals, the effects of such disorder can only be investigated by making the material even less perfect - but in a controlled way. In the work described here we have created isolated point defects uniformly through the $25\,\mu m$ samples using 5 MeV proton irradiation[8]. In this case a vacancy-interstitial pair is produced by a Coulomb collision between the proton and a nucleus in the material. Since the protons pass completely through the sample, the effects observed come entirely from the increased number of defects - not from implanted hydrogen.
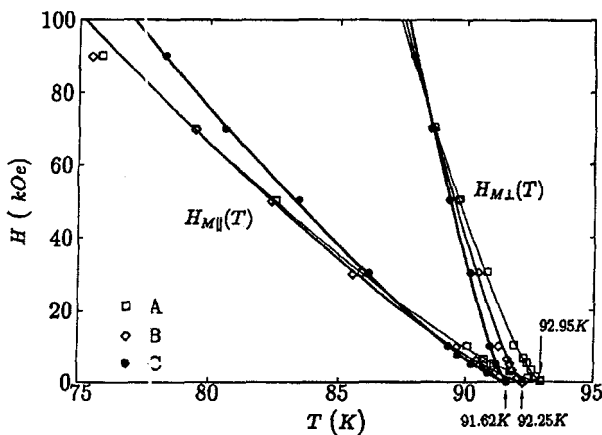

Figure 11: The vortex-solid melting transition lines for the magnetic field, H, parallel to and perpendicular to the c axis of the crystal for samples A, B, C. The solid lines are fits using parameters described in Table 2 for a formula given in Section IV of the text[8].

In Fig. 11 we see the effect on the vortex-solid melting lines for the axis of the crystal. In magnetic field parallel to and perpendicular to the this figure sample

A has not been irradiated and B and C were irradiated by 5×10^{15} and 10^{16} protons/cm², respectively. The solid lines are from the expression:

$$H_{M(T)} = H_{M(O)}|1 - (T/T_{co}|^{2\nu_0} , \qquad (7)$$

where the parameters are given in Table 2.

For magnetic fields from 1 to 90 kOe, we find that there is second-order melting transition despite the increased number of point defects from the irradiations (~ 2 per μm per proton). The vortex transport properties near the melting transition are seen to be governed by the same critical exponent ($\nu_0 \simeq 2/3$) for all three samples. The transition temperature at zero field, T_{co}, drops slightly with increasing fluence.

In Fig. 12 we plot the limiting current density J_x versus reduced temperature (T/T_{co}); above J_x the superconducting system is in the flux-flow regime with ohmic vortex dissipation. In this limit $J_x(T)$ is proportional to $|1 - (T/T_{co})|^{\nu_0}$. The last column in Table 2 shows that the exponent, a, that best fits J_x is indeed approximately equal to ν_0.
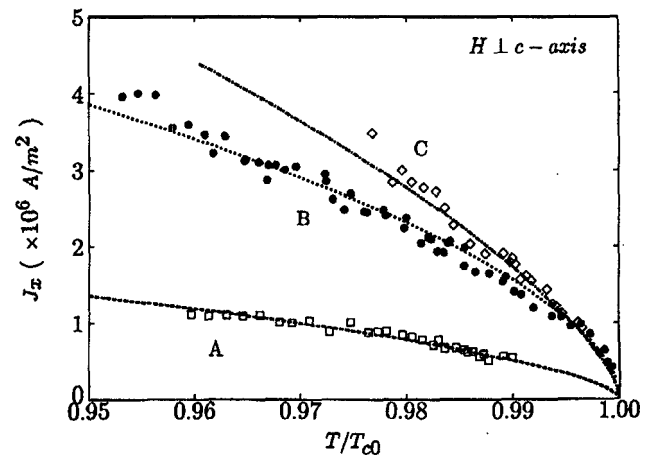

Figure 12: The flux-flow crossover current density (J_x) is plotted versus the reduced temperature (T/T_{co}) for samples A, B, C with the magnetic field perpendicular to the c axis of the crystal. The dotted lines are fits to the data with $J_x(T)$ proportional to $|1 - (T/T_{co})|^a$. (Note that J_x is independent of the magnetic field.) [8].

This work in only the first stage in our attack on the problem. At the present time we are proceeding in two ways: the first is that small crystals without twin planes have been obtained from IBM, these will remove the effect of those imperfections from the measurements; the second is that samples have been irradiated with GeV heavy ions in order to produce continuous tracks

550 T. A. Tombrello

Table 2: The effect of 5 MeV proton fluence on the zero-field transition temperature T_{co}, the critical field exponents $\nu_{0\parallel}$ and $\nu_{0\perp}$ power "a" for the flux-flow crossover current density, J_x.

Sample	ϕ (protons/cm^2)	T_{co} (K)	$\nu_{0\parallel}$	$\nu_{0\perp}$	a
A	0	92.955 ± 0.05	0.65	0.65	0.62
B	$\sim 5 \times 10^{15}$	92.25 ± 0.05	0.63	0.64	0.58
C	$\sim 10^{16}$	91.62 ± 0.05	0.62	0.63	0.67

of damage through the crystals, thereby giving more substantial pinning sites for the flux lines. Since such columnar defects can also be oriented as desired with respect to the axes of the crystal, this should allow us to separate the effects of the natural anisotropy of the crystals from those introduced by the defects.

V. Conclusions

In this paper I have given samples of recent accomplishments in our laboratory that indicate what we think are major trends in this area of research. It has always been the case that using ion beams provides opportunities for both the analysis/characterization of materials as well as modifying their properties. With regard to the former, it seems clear that TOF detection techniques will extend the use of RBS because it overcomes the limitations of surface barrier detectors for both heavy ions and low energy ions. In the case of materials modification, these examples show that modification can be accomplished without introducing a foreign species and that even the damage left by the ion can produce remarkable effects.

References

1. M. Dobeli, P. C. Haubert, R. P. Livi, S. J. Spickelmire, D. L. Weathers, and T. A. Tombrello, Nucl. Instr. Meth. B47, 148 (1990).

2. M. Dobeli, P. C. Haubert, T. A. Tombrello, J.-I. Chyi, D. Huang, and H. Morkoç, Nucl. Instr. Meth. B52, 71 (1990).

3. T. Venkatesan, R. P. Livi, T. C. Banwell, T. A. Tombrello, M.-A. Nicolet, R. Hamm, and A. E. Miexner, *Ion* Beam Processes in Advanced Electronic Materials and Device Technology, eds. F. H. Eigen, T. W. Signan, and B. R. Appleton, *Materials* Research Society Symposia Proceedings, Volume 45, 189, (Materials Research Society, Pittsburg, 1983).

4. M. Dobeli, T. J. Jones, A. Lee, R. P. Livi, and T. A. Tombrello, Rad. Eff. Def. in Solids 118, 325 (1991).

5. N. F. Mott, Conduction in Non-Crystalline Material~(Clarendon Press, Oxford, 1987).

6. A. Hedin, P. Hakansson, B. Sundqvist, and R. E. Johnson, Phys. Rev. B31, 1780 (1985).

7. D. B. Gingold and C. J. Lobb, Phys. Rev. B42, 8220 (1990).

8. W. Jiang, N.-C. Yeh, D. S. Reed, U. Kriplani, T. A. Tombrello, A. P. Rice, and F. Holtzberg, Phys. Rev. B47 in press.